Materials & Design 244 (2024) 113113

Contents lists available at ScienceDirect

Materials & Design

journal homepage: www.elsevier.com/locate/matdes

Radial dependence of thermal, structural and micro deformation characteristics in Cu-Zr-Al bulk metallic glass subjected to high pressure torsion

Talaye Arjmandabasi [a], Ádám Révész [a,*], Viktória K. Kis [b,c], Dávid Ugi [a], Erhard Schafler [d], Zsolt Kovács [a]

[a] Department of Materials Physics, Eötvös Loránd University ELTE, H-1117 Pázmány Péter st. 1/A, Budapest, Hungary
[b] HUN-REN Centre for Energy Research, Institute of Technical Physics and Materials Science, H-1121 Konkoly-Thege Miklós út 29-33, Budapest, Hungary
[c] Department of Mineralogy, Eötvös Loránd University, H-1117 Pázmány Péter sétány 1/c, Budapest, Hungary
[d] Faculty of Physics, University of Vienna, A-1090, Boltzmanngasse 5, Vienna, Austria

ARTICLE INFO

Keywords:
Bulk metallic glass
Glass forming ability
Micropillar
Microcompression
Acousticemission

ABSTRACT

Disk of a $Cu_{38}Zr_{54}Al_8$ bulk metallic glass was subjected to severe plastic deformation by high pressure torsion up to 25 revolutions. X-ray diffraction was utilized to investigate the microstructure of the deformed sample, while the thermal behavior of the glass was analyzed by differential scanning calorimetry. To examine the effect of plastic straining on structural changes, micropillars were fabricated on the cross-section of the disk along the radius at specific locations, i.e. center, half radius and perimeter. Compression tests of these micropillars were conducted in a scanning electron microscope with simultaneous recording of continuous acoustic emissions. Present paper captures the effect of competition between thermal relaxation and deformation induced structural changes. Specifically, probability distributions were constructed for a series of acoustic emission events, revealing that the occurrence of acoustic emission bursts at larger deformations is in correlation with the shift of the X-ray diffraction halos and change in thermal characteristics. Accordingly, a transition was identified from random to correlated acoustic emission behavior parallel with a progressive increase in the accumulation of excess free volume from negative to positive values.

1. Introduction

Disordered amorphous structures and distinct mechanical characteristics of metallic glasses (MGs) have attracted significant attention in recent decades [1]. MGs can be formed in massive form via rapid quenching by copper mold casting by surpassing crystallization during solidification resulting in bulk metallic glasses (BMGs) [2]. The outstanding properties of BMGs include high tensile strength, superior elasticity and good wear and corrosion resistance [1,3], however, they usually exhibit negligible ductility, resulting in catastrophic fracture upon tension, compression and bending experiments. All these positive and negative features are directly related to the absence of structural defects down to sub-nanoscale [4].

Tailoring the microstructure and mechanical behavior of BMGs is crucially determined by the composition of the glassy alloy [5,6]. Zr-based [7,8] and CuZr-based [9,10] BMGs have been in the forefront of basic and applied research, since they are built-up from inexpensive components and exhibit enhanced thermal stability, high glass forming ability (GFA) [10] and intrinsic plasticity [11,12]. The Cu-Zr binary system possesses such a high GFA that facilitates to cast the alloy into a bulk glassy form in wide composition range [13]. Thermal annealing below the glass transition (T_g) of a CuZr-based BMG yields an increase in its thermal stability [12], while another CuZr-based BMG with extreme high stability (Vitreloy) shows a wide supercooled liquid range (SCLR) [14]. Isothermal pre-annealing in the SCLR results in the increase of the viscosity via the formation of nano-quasicrystals.

In order to enhance the ductility of BMGs by dispersing the macroscopic external strain among a large number of localized plastic events and large number of shear bands, severe plastic deformation (SPD) methods can be applied by incorporating surface constraints [15–18]. Among the large variety of different SPD techniques, high-pressure torsion (HPT) exhibits the highest equivalent strain [19]. During HPT

* Corresponding author.
E-mail address: revesz.adam@ttk.elte.hu (Á. Révész).

https://doi.org/10.1016/j.matdes.2024.113113
Received 17 April 2024; Received in revised form 5 June 2024; Accepted 21 June 2024
Available online 22 June 2024

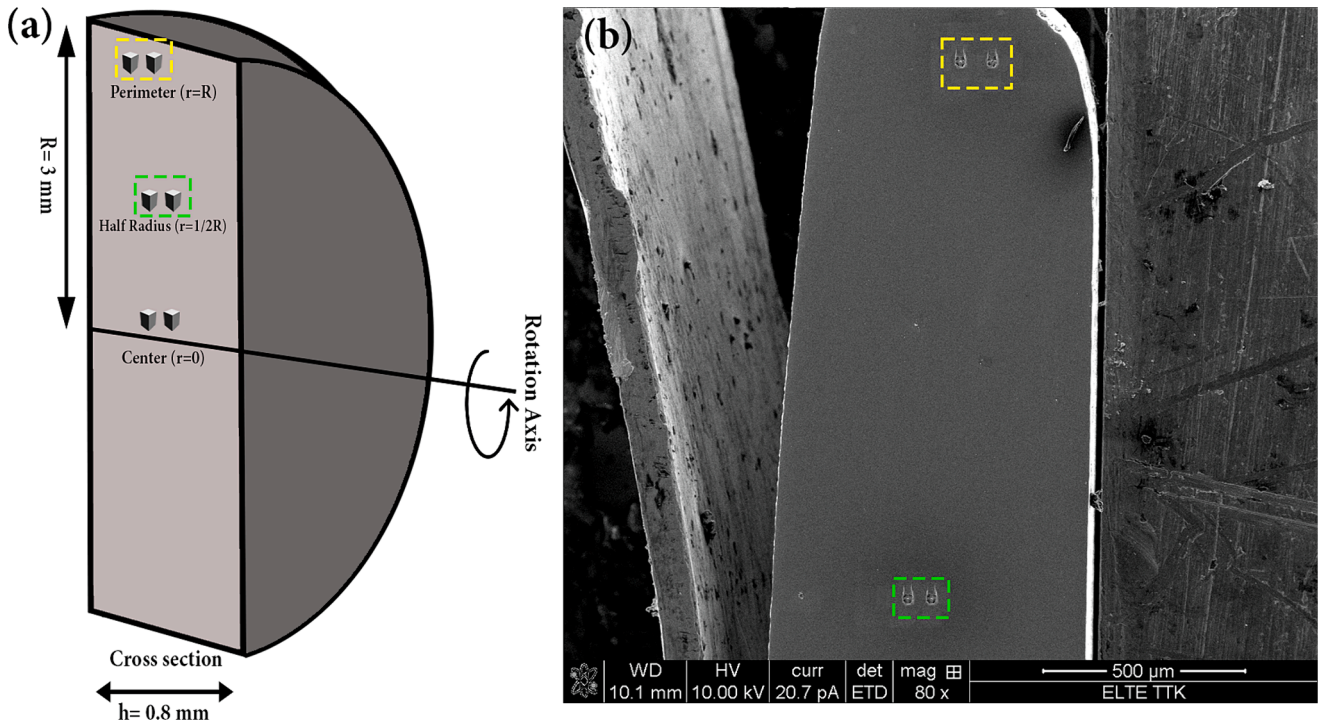

Fig. 1. (a) Schematic of the cross section of the HPT disk showing different sectors and pillars locations. (b) SEM image taken on the cross section of the disk showing the location of pillars made on the perimeter (r = R) and half radius (r = ½ R).

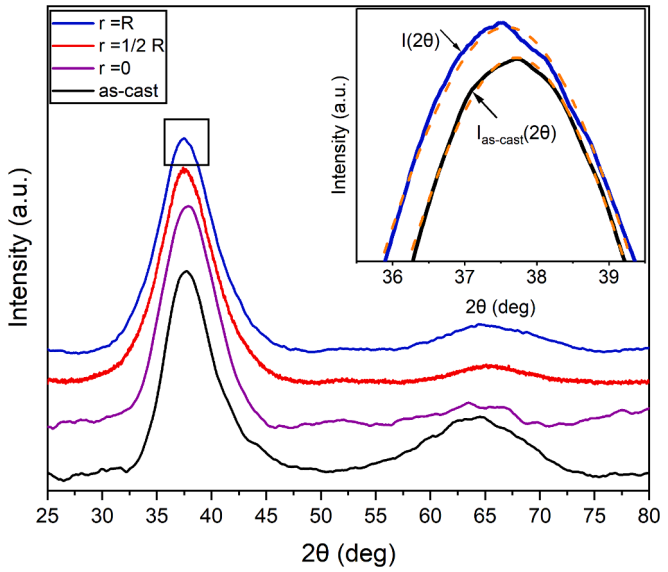

Fig. 2. The XRD pattern corresponding to the as-cast Cu38Zr54Al8 BMG and different sectors of the HPT-disk. Inset shows the vicinity of the first halo with the Gaussian- fit confirming the shift of its maxima due to SPD.

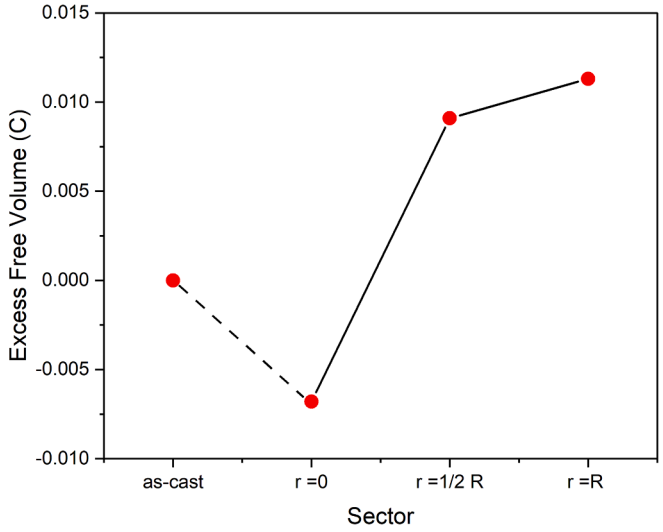

Fig. 3. Excess free volume (C) corresponding to different sectors of the HPT-disk.

a thin, disk-shaped specimen is subjected to simultaneous pressure and torsional shear deformation between two stainless steel anvils [20,21]. Applying HPT on MGs and BMGs can significantly enhance their plasticity [22], additionally, this deformation process can provoke structural changes in the glass, such as change in microstructure, development of free volume and anisotropy. [23–26]. By analyzing the changes in the pair distribution functions, it is assumed that structural rejuvenation can take place during severe plastic deformation in HPT [27]. Molecular dynamic simulations have shown that shear bands can be suppressed and constrained during HPT in a $Cu_{50}Zr_{50}$ glass, resulting in "forced cooperative flow" [28]. Applying nanoscale strain mapping on a $Zr_{50}Cu_{40}Al_{10}$ metallic glass subjected to HPT, it was found that the local structure was distorted in various directions with various intensities, whereas the overall structure was distorted along the rotational direction [29].

By analyzing the radial variations along the diameter of a HPT-processed BMG-disk, a detailed insight into the spatial and strain-dependent anisotropic microstructural features and mechanical properties of the glass can be explored. For instance, the Young's modulus of a CuZr-based disk has remarkable decrease as a function of the radial distance from the rotation axis [30]. This trend is mainly attributed to the increase in the free volume due to the nucleation and propagation of shear bands [31]. In-situ synchrotron studies supported that there exists

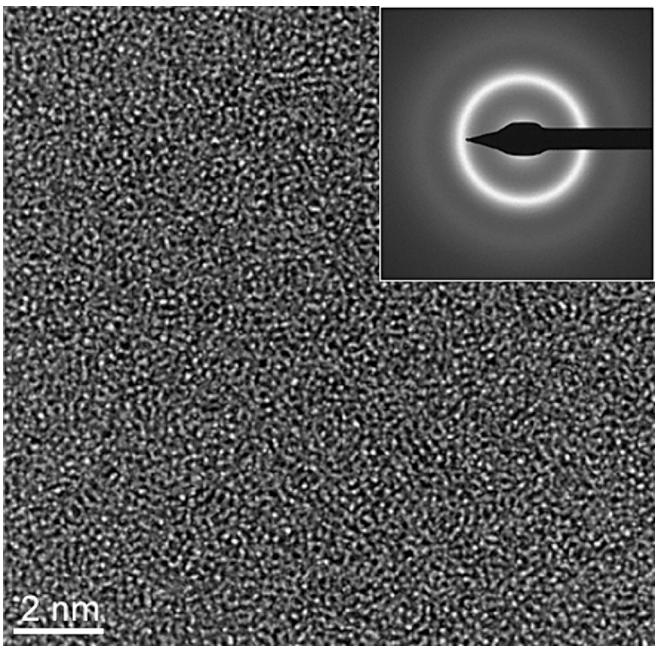

Fig. 4. HR-TEM and the corresponding SAED (insert) taken on the cross section at the perimeter (r ~ R) of the HPT-disk.

a varying structural anisotropy along the radius of a HPT-deformed CuZr-based BMG [25]. Molecular dynamics simulations also confirmed the variation of the local atomic structure, i.e. a transition of icosahedral units into other type of clusters of a $Cu_{50}Zr_{50}$ glass was obtained from perimeter to center of the sample during torsion deformation [32]. When the applied shear strain exceeds a critical value, a crystalline-amorphous transition can take place, resulting in enhanced hardness of the amorphous phase at the periphery of the disk [33]. On the other hand, HPT is also capable to promote deformation dependent nanocrystallization, especially in glasses with lower GFA [34]. The size and volume fraction of these deformation induced nanocrystals are significantly different at the center and periphery of a CuZr-based HPT-disk, in correlation with the total crystallization enthalpy release [35]. At the same time, an abrupt transition occurs in the morphology when flakes of a rapidly quenched MG ribbon is deformed by HPT. Namely, the flakes embedded in the amorphous matrix close to the center transform into thin lamellae at the perimeter, due to the extreme large and mostly homogeneous shear deformation in the outer region [36]. Creep tests by Ebner et al. have pointed out that HPT-deformed CuZr-based alloy exhibits increase in total creep with respect to its as-cast counterpart and a strong spatial correlation develops along the cross-sectional area, caused by a gradient structure. In addition, an increase in the fraction of the rejuvenated amorphous volume was also observed as the radial distance from the center of the disk increases [37]. Applying synchrotron radiation in transmission on a high stability Zr-based Vitreloy1b BMG subjected to severe plastic shear deformation by HPT reveals the absence of any nanocrystallization, independent of the local strain [38]. In addition, the radial dependency is evidenced by the monotonously increasing shift in the position of the first diffraction halo, indicating a gradual structural change along the radius of the HPT disk [38]. 2-dimensional mapping of the disk confirmed the change of the average effective volume. A volume decrease at the center of the deformed disk was observed, analogously to a relaxed state of an as-cast glass, nevertheless, a larger effective volume was detected at higher deformation [26]. The extreme stability of Zr-based BMGs against crystallization in the whole volume of a HPT-disk was also confirmed by calorimetry [39].

In absence of high hydrostatic pressure, deformation in BMGs exhibits severe strain localization and accompanied synchronization of localized plastic events. Acoustic emission (AE) signal can describe these dynamically synchronized events as they emit elastic waves during structural stress relaxation [40,41]. Since AE events precede macroscopic stress relaxation [42] and AE detection collects data with microsecond time resolution from the emitted acoustic events, the

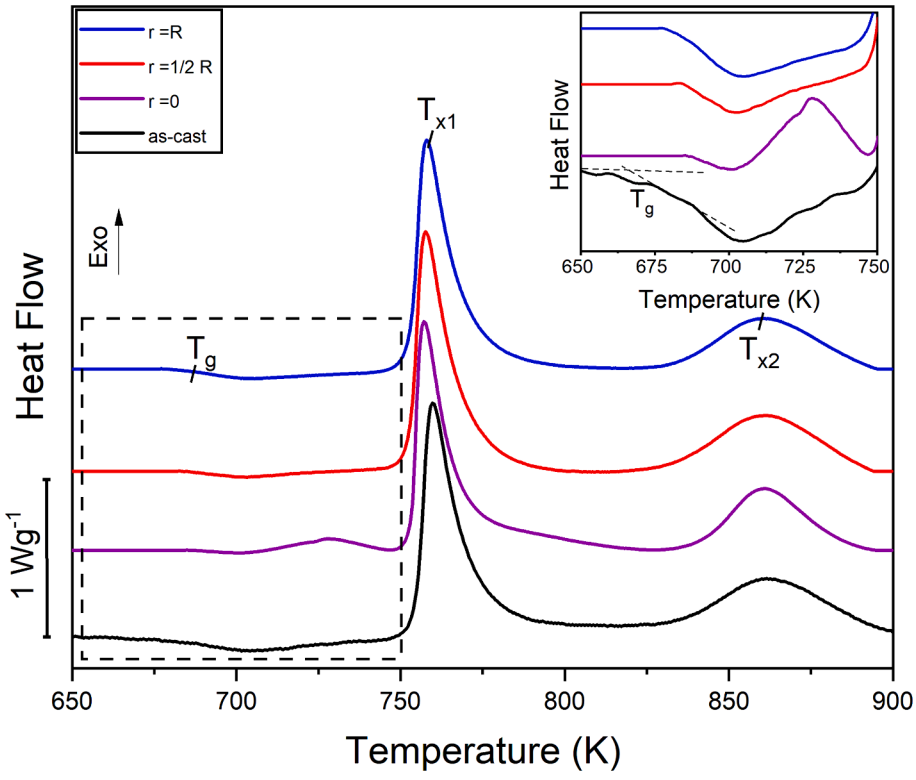

Fig. 5. DSC curves of the as-cast BMG and different sectors of the HPT-disk obtained at the heating rate of 20 K/min.

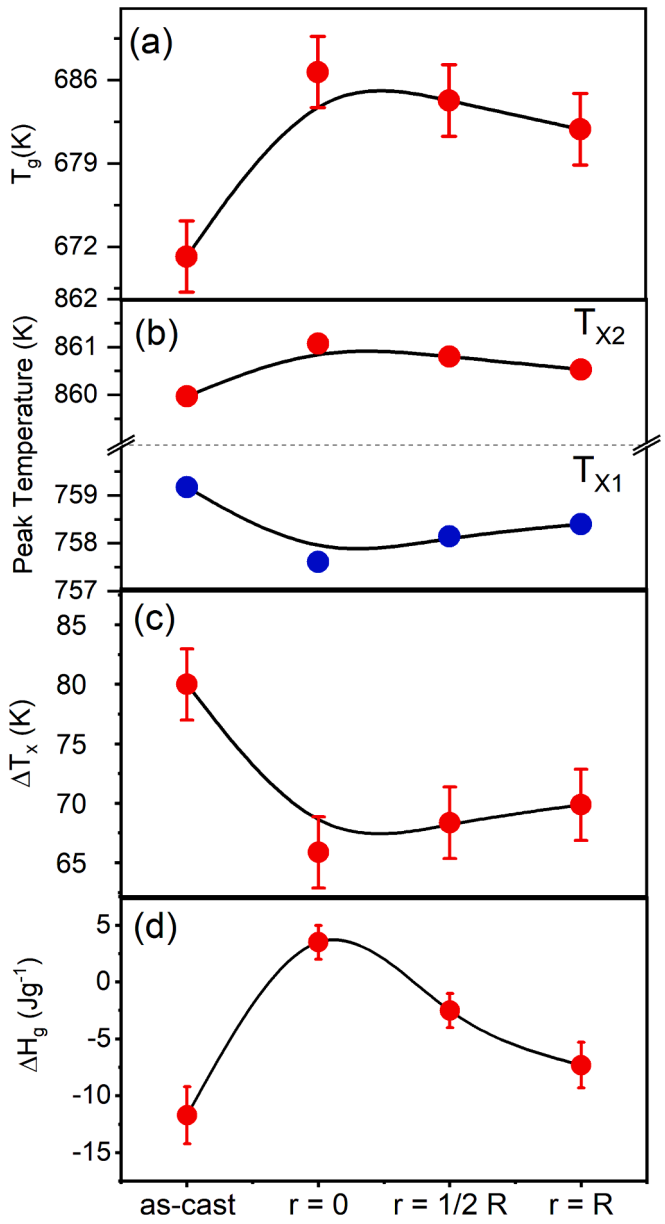

Fig. 6. (a) glass transition temperature (T_g), (b) crystallization peak temperatures (T_{x1} and T_{x2}), (c) width of the supercooled liquid region (ΔT_x) and (d) the integrated enthalpy (ΔH_g) of the SCLR for the as-cast BMG and different sectors of the HPT-disk.

experimentally recorded AE signal accounts for the structural rearrangements and provide unique dynamic information on shear band formation in metallic glasses [43,44]. Statistical analysis of the time evolution of such AE events in plastically deformed BMG provided evidence on the formation of AE event bursts [45]. It was demonstrated that sample size have a strong effect on shear localization in metallic glasses, for example, deformation tests on sub-micron sized micropillars exhibit plasticity or even homogeneous flow [44–48]. For micrometer size pillars of MGs, generally, shear bands form during straining. However, the deformation in these shear bands can be stabilized temporarily by elastic interaction between the micropillar and the indenter [49–51]. Recently, AE detection was carried out for crystalline [52] and BMG micropillars [53] and a coincidence was observed between the timing of AE events and plastic events [53].

Metallic glass structure can be tuned in terms of free volume content towards either negative (relaxation) or positive (rejuvenation) directions. In a single HPT experiment, spectrum of such glassy structures can be obtained as a function of radial position [26]. Since these structural variations can effectively change plastic deformation [22], the dynamic behavior in microplastic experiments is targeted presently to reveal connection between the structural variation and synchronization of plastic events. Therefore, a series of micropillar compression tests coupled with simultaneous AE detection were carried out and reported in the present paper. The micropillars were fabricated from a high GFA $Cu_{38}Zr_{54}Al_8$ BMG subjected to HPT up to extreme shear deformations. AE events due to the micro deformation are analyzed statistically for pillars in located at different positions along the diameter of the HPT disk. Radial variations of thermal and structural characteristics of the HPT-deformed BMG disk are discussed and compared to changes in the statistical behavior of AE events.

2. Experimental methods

2.1. Sample preparation

A BMG cylinder of $Cu_{38}Zr_{54}Al_8$ nominal composition and a radius of R = 3 mm was fabricated by suction casting into a Cu mold using an arc furnace operating under a protective argon atmosphere. Details of sample preparation can also be found in [53,54]. Subsequently, disks with an approximate thickness of h = 0.8 mm were cut from the as-cast cylinder. Afterwards, these disks were exposed severe plastic deformation by high-pressure torsion with N = 25 number of complete turns with the angular velocity of ω = 0.2 revolution/min at room temperature under the applied pressure of 8 GPa. The accumulated shear strain (γ) for torsion deformation at a radius r can be given by [21],

$$\gamma(r,N) = \frac{2\pi Nr}{h} \quad (1)$$

Accordingly, the achieved strain by HPT at the perimeter of the disk can reach exceptionally high values: $\gamma \approx 600$. For further investigations the HPT-disk was cut along its diameter and the cross section was manually polished to 50 nm using Al_2O_3 powder. In order to explore any possible strain dependent variation along the cross section, three distinct sectors were taking into account, as illustrated schematically in Fig. 1a. Hereafter these regions will be denoted as r = 0 (center), r= ½ R (half radius) and r = R (perimeter).

2.2. X-ray powder diffraction

The atomic-level microstructural analysis of the as-cast BMG and the cross section of the HPT-disk was performed on a high resolution double crystal X-ray powder diffractometer (XRD) applying monochromatic Cu Kα radiation (λ = 0.154 nm) with negligible instrumental broadening. The small spot size of the X-ray beam (100 × 300 μm^2) enables high spatial resolution along the cross section of the HPT-disk. The device was equipped with a fine focus rotating copper anode (Rigaku Multmax-9) operating at 40 kV and 100 mA. Scattered photons were detected by a static imaging plate, where high precision was maintained in the imaging plate positioning between the subsequent measurements. The 2-dimensional patterns registered by the imaging plate were integrated after spatial distortion correction. Data acquisition spanned in the range of 2θ = 25–80°.

2.3. Transmission electron microscopy

For high-resolution transmission electron microscopy (HR-TEM) study the sample was prepared using focused ion beam (FIB) milling (FEI Scios 2 DualBeam System). The HR-TEM analysis was performed using a FEI Themis 200 G3 transmission electron microscope with a Cs corrected objective lens (FEG, point resolution is around 0.09 nm in HR-TEM mode) operating at 200 kV. Selected area electron diffraction (SAED)

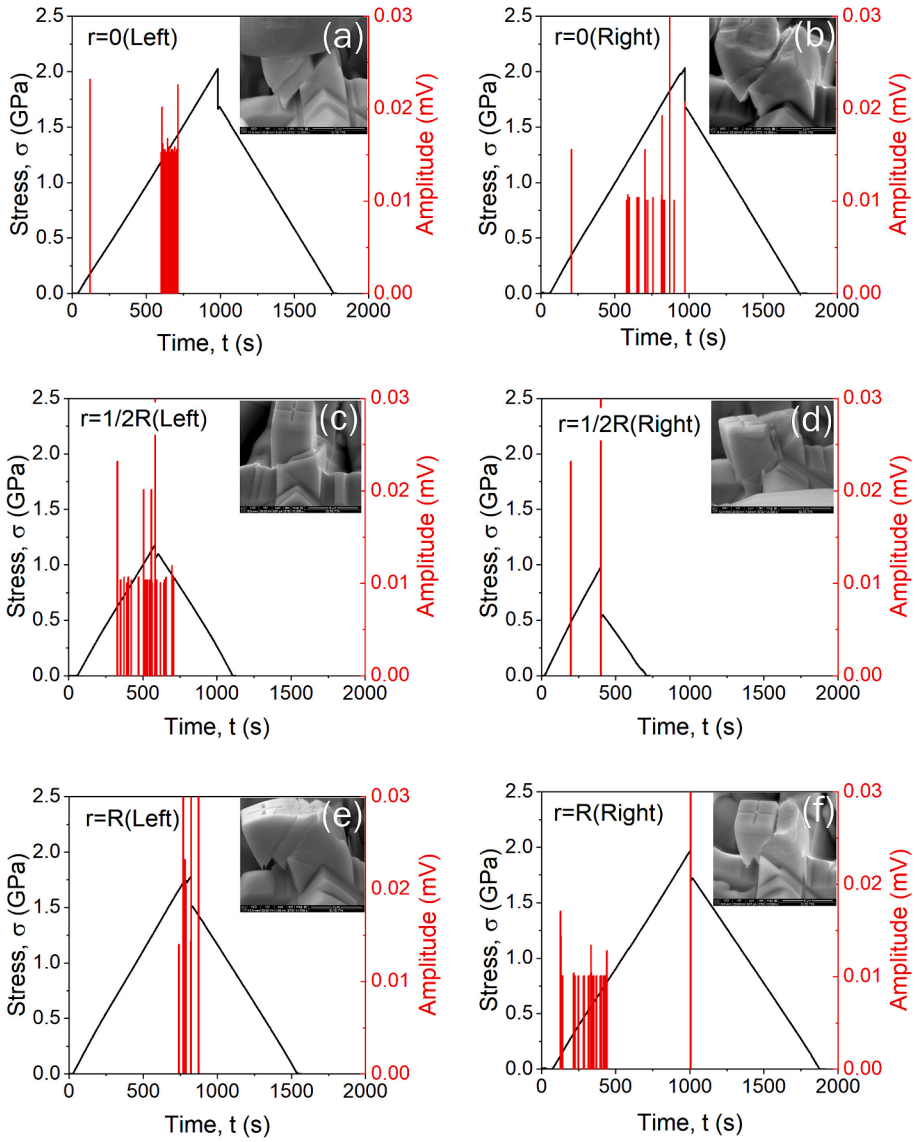

Fig. 7. Correlation between serrations of the deformation curves (black) and the amplitudes of the acoustic emission events (red) in micropillar compression tests for 4 μm pillars of HPT deformed samples at r = 0, r= ½ R and r = R. Insets show the SEM images of the corresponding micropillars after plastic deformation and unloading. (For interpretation of the references to colour in this figure legend, the reader is referred to the web version of this article.)

pattern was taken from an area of approximately 650 nm diameter, following standardized procedure allowing 0,1% accuracy without internal standard. Further details of the sample preparation procedure are reported in a previous work [55].

2.4. Differential scanning calorimetry

For thermal investigations, a half of the HPT-disk was fragmented into three parts according to their distance from the torsion axis. Measurements on these fragments as well as on the as-cast BMG was carried out on a Perkin Elmer power-compensated differential scanning calorimeter (DSC). A linear heating ramp with a scan rate of 20 K/min was applied in all measurements. Enthalpy of the SCLR (ΔH_g) was calculated as the integral of the DSC-signal after baseline substraction. All experimental procedures were conducted under a controlled Ar atmosphere. Calibration of temperature and enthalpy was performed using pure In and Al.

2.5. Pillar fabrication, compression and acoustic emission detection

Micropillars were fabricated in both the as-cast and HPT deformed samples to facilitate localized mechanical tests. After surface polishing of the cross section of a BMG-slice and HPT-disk, an acetone wash was performed. Afterwards, micropillars were prepared on these polished surfaces by Ga ion milling with FIB inside a FEI Quanta 3D dual-beam scanning electron microscope (SEM) under vacuum conditions. The locations of the micropillars on the cross section of the HPT-disk was chosen at r = 0, r= ½ R, r = R. Two pillars were fabricated close to each other in each sector to get insight into the repeatability of the mechanical tests, see the corresponding SEM image in Fig. 1b. The milling process yields square-shaped pillars with an edge length of a = 4 μm and a corresponding height (L), achieving an aspect ratio of approximately L/a = 2. Before this process, a thin Pt cap was deposited onto the top of each micropillar to minimize Ga ion contamination during milling. Subsequently, the pillars were produced through FIB milling in the same SEM by gradually reducing the ion current. Deformation tests were performed in-situ with an on-site built nanoindenter device in the same SEM equipment coupled with continuous AE detection [52,56]. During

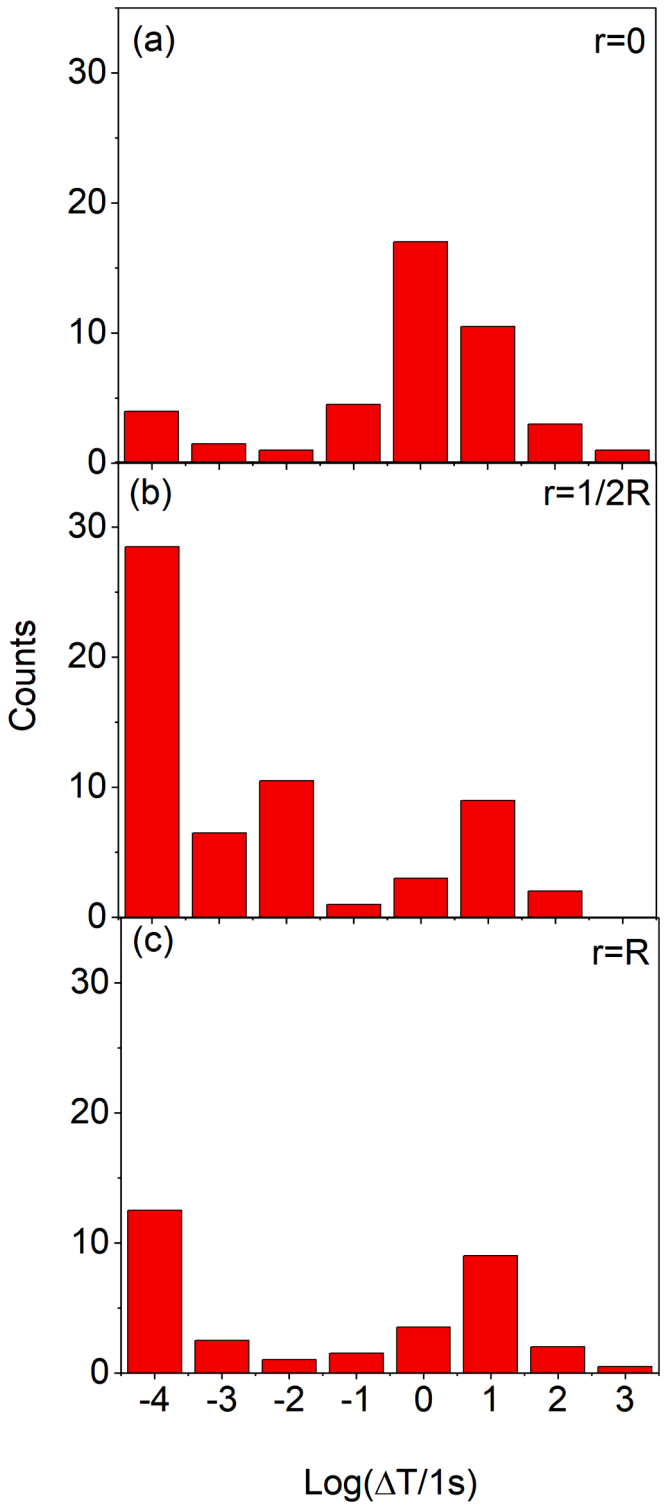

Fig. 8. AE event counts vs. the log of waiting time (ΔT).

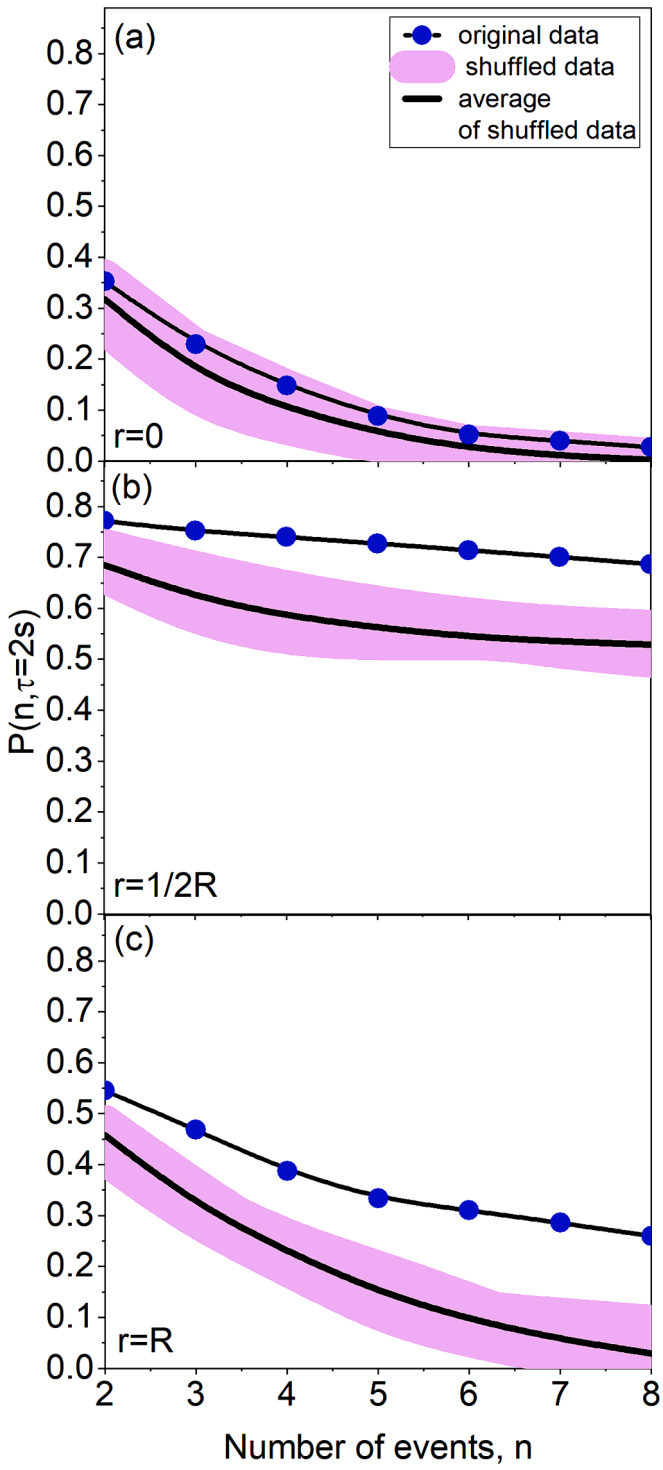

Fig. 9. Probability distribution of a sequence of n events for the two experimental (original) datasets and randomized one (shuffled data) presented as a function of number of events.

micro compression tests, micropillars were compressed with a doped flat head diamond indenter, which was attached to the platen of the in-situ indenter by a soft elastic spring. The platen velocity of the indenter was set to 10 nm/s. Indenter displacement was determined from the platen position and from the elastic length change of the spring [52,53]. In each micro compression test, indenter movement was reversed in a few seconds after plastic regime was reached (plasticity was observed in the SEM) and then the pillar was unloaded completely.

3. Results

3.1. Structural analysis

The XRD pattern of the $Cu_{38}Zr_{54}Al_8$ BMG shown in Fig. 2, presents two distinct halos at around $2\theta \sim 37^\circ$ and $2\theta \sim 64^\circ$. The presence of the first broad peak and the lack of sharp crystalline reflections refer to the fully amorphous nature of the alloy. As one can also notice, severe shear

deformation by HPT does not yield any drastic change in the diffractograms, independent of the local strain. The lack of any crystallization Bragg-peaks confirm the extreme structural stability of the amorphous alloy against external mechanical influence. The addition of Al to the high glass forming binary Cu-Zr can prevent the growth of crystalline embryos that might formed during fast cooling of the liquid alloy [54]. Nonetheless, a slight shift in the position of the main halo can be notices for all HPT-sectors with respect to the as-cast BMG. The inset of Fig. 2 presents the magnified vicinity of the more reliable first halo maximum for the as-cast glass ($I_{as\text{-}cast}(2\theta)$) and the peripheral region of the HPT-disk (I(2θ)). Indeed, a clear shift in the 2θ peak position towards lower values is visible for the deformed state.

In order to quantify the microstructural changes associated with the variation of the excess free volume content (C) along the cross section of the HPT-disk, the following formula was applied [57,58]:

$$C = 1 - \left(\frac{Q_{HPT}}{Q_{as-cast}}\right)^3 \quad (2)$$

where $Q = \frac{2\pi \sin\theta}{\lambda}$. The exact determination of the halo position was accomplished by fitting these halos with a Gaussian function, see also Fig. 2 inset. As can be seen from Fig. 3, the excess free volume content dropped below value of the as-cast BMG in the center of the HPT disk and shows a notable and monotonous increase along the disk radius, changing from C = −0.7 % at r = 0 to C = 1.2 % outward to r = R. Precisely, these changes report only about an excess free volume change in the sense that, in a multicomponent glass, the halo maxima reflect only the weighted average of the different atomic contribution.

The disordered nature of the most deformed peripheral region of the HPT-disk was undoubtedly confirmed by the HRTEM study presented in Fig. 4. The lack of any contrast and visible atomic planes in the micrograph and the presence of several diffuse halo in the corresponding SEAD pattern indicate a homogeneous fully amorphous structure.

3.2. Thermal analysis

Linear heating calorimetric thermogram of the as-cast $Cu_{38}Zr_{54}Al_8$ BMG obtained at 20 $Kmin^{-1}$ exhibits the typical features of a glass, including the glass transition (T_g = 671 K) followed by two distinct exothermic crystallization transformation peaks (T_{x1} = 759 K and T_{x2} = 860 K), see Fig. 5. The high T_g and large value of SCLR (ΔT_x = 80 K, where $\Delta T_x = T_{x1,\ onset} - T_g$) confirms the extremely high GFA of the Cu-Zr-Al system [59]. Detailed thermal investigation of this alloy was presented in an earlier study [54].

In addition to outstanding structural stability (see Figs. 2 and 4), the $Cu_{38}Zr_{54}Al_8$ glassy alloy possesses remarkable thermal stability against extreme shear deformation, as confirmed by the DSC curves of the different sectors of the HPT-disk (Fig. 5). Each thermogram of the deformed states is very similar to that of the as-cast glass, presenting T_g and the subsequent T_{x1} and T_{x2} transformations. The inset of Fig. 5 depicts the endothermic glass transition region, with a slight increase in T_g due to the severe plastic deformation.

Quantitative analysis of the characteristic values obtained from the DSC measurements are summarized in Fig. 6. As one can realize form Fig. 6a, T_g undergoes a ~15 K increase due to torsion. Since T_g is one of the key GFA parameters [1], it is concluded that the thermal stability of the $Cu_{38}Zr_{54}Al_8$ glassy alloy is improved by exposing the material to HPT. As it is also seen in the figure, T_g varies slightly with increasing deformation along the radius of the disk. The minor variation in T_{x1} and T_{x2} peak crystallization temperatures confirms again that $Cu_{38}Zr_{54}Al_8$ glass is extremely stable alloy against extreme plastic deformation illustrated in Fig. 6b. For example, the decrease in T_{x1} is less than 2 K for the HPT sample, irrespectively from the magnitude of the shear strain. As we approach the perimeter of the disk (r = R), a marginal increase occurs when compared to the center (r = 0). Conversely, the T_{x2} characteristic temperature presents an opposite behavior, i.e. a slight increase is observed for the HPT-disk, while a downward trajectory takes place at larger distance from the center of the disk. Fig. 6c illustrates ΔT_x for the as-cast BMG and the different HPT-sectors. As one can see, the ΔT_x parameter, which is more responsible for the stability of the supercooled liquid, decreases slightly from 80 K to 65 K-70 K after severe shear deformation. Nevertheless, the deformed glass still exhibits a remarkable GFA and thermal stability, especially at the perimeter (r = R). Similar to the variation of excess free volume determined for X-ray experiments (see Fig. 3), the integral of the DSC-signal for the SCLR (ΔH_g) can also indicate structural changes between the different glassy states. As seen in Fig. 6d, the ΔH_g value shows a significant increase up to positive values for the center of the disk (r = 0) with respect to the as-cast BMG. At higher deformation states (r= ½ R and r = R) ΔH_g decreases monotonously down to negative values. Here we note that the ΔH_g values have relatively large uncertainty and they contain contributions also from the heat capacity difference between the glass and the supercooled liquid states.

3.3. In-situ micro deformation tests with acoustic emission detection

As illustrated in Fig. 7(a-f), the applied stress and the simultaneously acoustic emission signal during compression is plotted as a function of time. The inset of each figure presents the corresponding SEM image taken on the pillars after the compression test. As seen, the deformation curves exhibit elastic–plastic behavior, including a linear elastic regime followed by smaller and larger stress drops in the plastic regime. Notably, a substantial stress drop is observed for all pillars within the plastic regime. However, this drop occurs more rapidly (approximately at 500 s, Fig. 7c and 7d) at r= ½ R compared to r = R (at around 1000 s, Fig. 7e and 7f). Accordingly, strong fluctuation can be observed in the yield strength comparing micropillars in different sectors. The yield strength of the r= ½ R pillars is about σ_{yield} = 1 GPa, while it is about σ_{yield} = 2 GPa at the perimeter and in the center of the HPT disk. The AE events illustrated in Fig. 7 signify the development of shear bands beyond the yield point, even extending into the elastic regime for $\sigma < \sigma_{yield}$. Additionally, the relationship between the AE amplitude and stress drop is highlighted in red in Fig. 7. (As a supplementary information on the dynamics of the micropillar deformation, a SEM image sequence of a deformation test is also available as Video 1). Major stress drops are in coincidence with the larger AE events for all sectors, except for the r = 0 (Left) pillar (Fig. 7a). Precisely, the significant acoustic emission events align with the load drops can be observed in the deformation curves. However, large number of minor evens can also be observed in the different samples at varying stresses within the elastic regime. These events seem to be correlated in time (see for example the event series at about 600 s in Fig. 7a).

To reveal the presence of these event series and handle large and small time differences equally, we computed the ΔT waiting time (the time difference between the subsequent events) and then calculated the distributions of the $\log_{10}(\Delta T)$ with equal binning. Fig. 8 shows these distributions (precisely the sum of the counts from the left and right pillars obtained for each sector). The plot demonstrates a substantial variability in event duration, ranging from $\Delta T = 10^{-4}$ s to $\Delta T = 10^{3}$ s. Fig. 8a illustrates a span of seven orders of magnitudes in waiting times for the r = 0 pillars, with a significant concentration of events occurring around $\Delta T = 10^{0}$ s. Accordingly, the waiting times are mostly occurring in the range of 0.1 s up to 10 s. Noteworthy this significant event concentration is less pronounced for the pillars located at r= ½ R and r = R, instead a strong peak occurs at very short time differences at around $\Delta T = 10^{-4}$ s, see Fig. 8b and 8c, respectively. This evaluation indicates a radial dependency of the AE event series as we approach the perimeter of the HPT-disk.

To assess the temporal correlations of AE events, we conducted a statistical analysis by calculating the probability distribution of the number of events (n) within the same burst, considering an arbitrary inter-event time parameter (τ). Because of the lack of large number of AE

events, the two tests obtained for the same sector were unified into a single data series. The evaluation was conducted using this unified data set (experimental data) and several randomized data series with the same ΔT distribution (shuffled datasets). For further details of this evaluation procedure see Ref [60]. In brief, this method provides insights into the probability of a series of n events, which have smaller event time differences than the τ parameter. In the present study we considered n = 8 events and τ = 2 s. Thereafter we determined that an event series (with a length of n) is a kind of event burst with large number of successive events during a short period of time. Fig. 9 shows these special probability distributions of the original experimental data (blue dots) and five shuffled datasets (purple region) for the different sectors. Difference between the original and the average of the randomly shuffled datasets (denoted by black line) can indicate the presence of such bursts of events in the AE signal. As evident from Fig. 9a, the original and shuffled data exhibit very similar exponential decay for the least deformed region of the HPT-disk (r = 0 position). On the other hand, a significant deviation is observed between the original and shuffled data for r= ½ R and r = R positions, see Fig. 9b and 9c, respectively. These observations align well with those in Fig. 8 and underscore a radial dependency of AE event distribution detected during compression of micropillars in a $Cu_{38}Zr_{54}Al_8$ HPT-disk.

4. Discussion

Minor changes in the structural and thermal characteristics of the HPT deformed $Cu_{38}Zr_{54}Al_8$ BMG with respect to the as-cast state arise from the attained maximum plastic deformation (see Eq. (1) and the applied deformation rate in the high pressure environment developed in the sample placed between the HPT-anvils. Plastic deformation, especially at high deformation rates, can induce structural changes (including structural inhomogeneities, phase separation or nucleation of crystalline embryos) in a highly stable glassy structure in competition with thermal relaxation [25,26,34,61]. This effect is often referred as the rejuvenation of the structure [27,37,62,63], when increase of sample volume or evolution of structural inhomogeneities may take place [38]. It is also known that sample volume increase stores more elastic energy and induces sensitive changes in the atomic mobility [64], leading to an increase of excess free volume of the non-periodic glassy structure [58]. However, this increased atomic mobility can easily transform the deformed glass into liquid state and induce thermal relaxation (melting of the glass) in the whole sample volume or mechanical relaxation (shear band formation) in highly localized regions [65]. Therefore, SPD is resulted in the increase of the excess free volume content of the glass in a typical deformation experiment.

In addition, experimental observations revealed that high hydrostatic pressure has an effect on the competition between the two processes, specifically visible change occurred in the inhomogeneity of shear bands formation during HPT process [23]. In present experiments, this combined effect, i.e. the interplay between the thermal relaxation and structural change are captured quantitatively, since the first XRD halo position indicates either decrease (r = 0) or increase (r= ½ R and r = R) in the excess free volume content in comparison to the as-cast state (see Figs. 2 and 3). The observed reduction of the excess free volume at r = 0 reports about a special glass state with very limited atomic mobility (see also ref. 26). This state, on the one hand, is similar to a thermally relaxed glass due to its reduced mobility, on the other hand, severe plastic deformation during the relaxation process has driven the glass in a structurally different state. This is also supported by the presence of a special exothermic peak within the SCLR for the r = 0 sector (see Fig. 5), which refers to the release of stored energy above the glass transition temperature (see Fig. 6d). Upon heating, this special glassy state tends to relax, however, this process occurs at higher viscosity of the glass, in accordance with the smallest free volume content of the r = 0 sector (see Fig. 3).

Shear band formation in these deformed states of low and high free volume content were further analyzed experimentally by in-situ micro-compression tests (see Fig. 7). Interestingly, the r = 0 sector performs different behavior if it is compared to the other two deformed states regarding the micro compression induced AE events (see Fig. 7). As was demonstrated, the majority of AE events with about ΔT = 1 s average waiting time can be observed in this state, while its distribution spreads over more equally several orders of magnitudes, covering the 10^{-4}-10^{3} s waiting time range (see Fig. 8). This effect is even more pronounced in Fig. 9, when the probability distributions are obtained for a sequence of n = 8 AE events. As was shown, the probability distribution for the r = 0 sector is practically in coincidence with the average of the shuffled distributions, which corresponds to a random behavior of the AE events. On the other hand, the probability plots indicate the existence of AE event series or AE bursts for larger deformations (r= ½ R and r = R), in coincidence with the larger free volume content (see Fig. 3), in a similar way as it was observed in free-end torsional experiments at ambient pressure [45].

5. Conclusions

Deformation dependence of the microstructure, thermal stability and micro-deformation characteristics were investigated on a $Cu_{38}Zr_{54}Al_8$ bulk metallic glass subjected to HPT. XRD analysis, HR-TEM imaging and calorimetry experiments confirmed the exceptional stability of the alloy against severe shear deformation. Shift in the positions of the main XRD halo indicates decrease in the center and increase toward the perimeter in the excess free volume in correlation with increasing plastic deformation in the HPT-disk.

Micro-compression tests with AE signal detection were performed along a radius of the deformed HPT-disk. Temporal behavior of the AE signal was investigated using a binning process to assess temporal delay between the consecutive events. Based on this evaluation, it is evident that events follow a random behavior for small deformation at the center of the HPT-disk. However, formation of AE event bursts is apparent in correlation with larger deformation and larger free volume content. This further emphasizes the effect of rejuvenation on the collective plastic behavior in BMGs.

CRediT authorship contribution statement

Talaye Arjmandabasi: Writing – original draft, Visualization, Methodology, Investigation, Data curation. **Ádám Révész:** Writing – review & editing, Investigation. **Viktória K. Kis:** . **Dávid Ugi:** Investigation. **Erhard Schafler:** Investigation. **Zsolt Kovács:** Writing – review & editing, Resources, Methodology, Formal analysis, Data curation, Conceptualization.

Declaration of competing interest

The authors declare that they have no known competing financial interests or personal relationships that could have appeared to influence the work reported in this paper.

Data availability

Data will be made available on request.

Acknowledgments

T.A. is indebted to the Tempus Public Foundation for providing a Stipendium Hungaricum Ph.D. scholarship. Dávid Ugi acknowledge the support of the postdoctoral excellence programme OTKA-PD-23 NKFIH-PD-146795 (D.U.). The authors are indebted to Prof. D.J. Browne for providing the BMG sample. TEM facility at HUN-REN Centre for Energy Research was supported by the grants no. VEKOP-2.3.3-15-2016-00002 and VEKOP-2.3.2-16-2016-00011 of the European Structural and

Investment Funds. Ms. Noémi Szász is acknowledged for preparation of FIB lamella.

Appendix A. Supplementary data

Supplementary data to this article can be found online at https://doi.org/10.1016/j.matdes.2024.113113.

References

[1] A. Inoue, Stabilization of metallic supercooled liquid and bulk amorphous alloys, Acta Mater. 48 (2000) 279–306, https://doi.org/10.1016/S1359-6454(99)00300-6.

[2] Y. Chen, C. Tang, K. Laws, Q. Zhu, M. Ferry, Zr-Co-Al bulk metallic glass composites containing B2 ZrCo via rapid quenching and annealing, J. Alloy. Compd. 820 (2020) 153079, https://doi.org/10.1016/j.jallcom.2019.153079.

[3] M.M. Trexler, N.N. Thadhani, Mechanical properties of bulk metallic glasses, Prog. Mater Sci. 55 (2010) 759–839, https://doi.org/10.1016/j.pmatsci.2010.04.002.

[4] G. Kumar, H.X. Tang, J. Schroers, Nanomoulding with amorphous metals, Nature 457 (2009) 868–872, https://doi.org/10.1038/nature07718.

[5] L. Shao, J. Ketkaew, P. Gong, S. Zhao, S. Sohn, P. Bordeenithikasem, A. Datye, R.M. O. Mota, N. Liu, S.A. Kube, Y. Liu, W. Chen, K. Yao, S. Wu, J. Schroers, Effect of chemical composition on the fracture toughness of bulk metallic glasses, Materialia 12 (2020) 100828, https://doi.org/10.1016/j.mtla.2020.100828.

[6] X. Han, I. Kaban, J. Orava, S.M. Das, V. Shtefan, M.V. Zimmermann, K. Song, J. Eckert, K. Nielsch, M. Herbig, Tailoring microstructure and properties of CuZrAl (Nb) metallic-glass–crystal composites and nanocrystalline alloys obtained by flash-annealing, J. Mater. Sci. Technol. 193 (2024) 253–266, https://doi.org/10.1016/j.jmst.2023.12.065.

[7] D. Fátay, J. Gubicza, J. Lendvai, Indentation creep behavior of a Zr-based bulk metallic glass, J. Alloy. Compd. 434–435 (2007) 75–78, https://doi.org/10.1016/j.jallcom.2006.08.103.

[8] J. Gubicza, J.L. Lábár, E. Agócs, D. Fátay, J. Lendvai, Effect of nano-quasicrystals on viscosity of a Zr-based bulk metallic glass, Scr. Mater. 58 (2008) 291–294, https://doi.org/10.1016/j.scriptamat.2007.10.002.

[9] D. Xu, B. Lohwongwatan, G. Duan, W.L. Johnson, C. Garland, Bulk metallic glass formation in binary Cu-rich alloy series – $Cu_{100-x}Zr_x$ (x=34, 36, 38.2, 40 at.%) and mechanical properties of bulk $Cu_{64}Zr_{36}$ glass, Acta Mater. 52 (2004) 2621–2624, https://doi.org/10.1016/j.actamat.2004.02.009.

[10] Á. Révész, A. Concustell, L.K. Varga, S. Suriñach, M.D. Baró, Influence of the wheel speed on the thermal behavior of $Cu_{60}Zr_{20}Ti_{20}$ alloys, Mater. Sci. Eng. A 375–377 (2004) 776–780, https://doi.org/10.1016/j.msea.2003.10.151.

[11] J.C. Lee, K.W. Park, K.H. Kim, E. Fleury, B.J. Lee, M. Wakeda, Y. Shibutani, Origin of the plasticity in bulk amorphous alloys, J. Mater. Res. 22 (2007) 3087–3097, https://doi.org/10.1557/JMR.2007.0382.

[12] X. Cui, X.F. Zhang, J.J. Li, F.Q. Zu, L.Z. Meng, J. Lu, F. Luo, Y.B. Ma, Centimeter-sized CuZrAl bulk metallic glass with good plasticity and chemical heterogeneity, Intermetallics 121 (2020) 106773, https://doi.org/10.1016/j.intermet.2020.106773.

[13] A. Zhang, D. Chen, Z. Chen, Bulk metallic glass-forming region of Cu–Zr binary and Cu–Zr based multicomponent alloy systems, J. Alloy. Compd. 477 (2009) 432–435, https://doi.org/10.1016/j.jallcom.2008.10.022.

[14] J. Lendvai, J. Gubicza, J.L. Lábár, Z. Kuli, Effect of crystallization on the deformation behavior of a Zr-based bulk metallic glass, Int. J. Mater. Res. 100 (2009) 439–442, https://doi.org/10.3139/146.110053.

[15] J. Sort, D.C. Ile, A.P. Zhilyaev, A. Concustell, T. Czeppe, M. Stoica, S. Suriñach, J. Eckert, M.D. Baró, Cold-consolidation of ball-milled Fe-based amorphous ribbons by high pressure torsion, Scr. Mater. 50 (2004) 1221–1225, https://doi.org/10.1016/j.scriptamat.2004.02.004.

[16] K. Edalati, I. Fujita, X. Sauvage, M. Arita, Z. Horita, Microstructure and phase transformations of silica glass and vanadium oxide by severe plastic deformation via high-pressure torsion straining, J. Alloy. Compd. 779 (2019) 394–398, https://doi.org/10.1016/j.jallcom.2018.11.086.

[17] R.D. Conner, W.L. Johnson, N.E. Paton, W.D. Nix, Shear bands and cracking of metallic glass plates in bending, J. Appl. Phys. 94 (2003) 904, https://doi.org/10.1063/1.1582555.

[18] M. Ezzeldien, Z.S. Kovács, J. Lendvai, F. Chmelík, K. Máthis, Stages in room temperature torsional deformation of a Vitreloy bulk metallic glass, J. Alloys Comp. 577 (2013) 25–29, https://doi.org/10.1016/j.jallcom.2013.04.103.

[19] K. Edalati, Z. Horita, A review on high-pressure torsion (HPT) from 1935 to 1988, Mater. Sci. Eng. A 652 (2016) 325–352, https://doi.org/10.1016/j.msea.2015.11.074.

[20] R.Z. Valiev, R.K. Ishlamgaliev, I.V. Alexandrov, Bulk nanostructured materials from severe plastic deformation, Prog. Mater Sci. 45 (2000) 103–189, https://doi.org/10.1016/S0079-6425(99)00007-9.

[21] A.P. Zhilyaev, T.G. Langdon, Using high-pressure torsion for metal processing: Fundamentals and applications, Prog. Mater Sci. 53 (2008) 893–979, https://doi.org/10.1016/j.pmatsci.2008.03.002.

[22] Á. Révész, Z.S. Kovács, Severe plastic deformation of amorphous alloys, Transactions 60 (2019) 1283–1293, https://doi.org/10.2320/matertrans.MF201917.

[23] Z.S. Kovács, E. Schafler, P. Szommer, Á. Révész, Localization of plastic deformation along shear bands in Vitreloy bulk metallic glass during high pressure torsion, J. Alloy. Compd. 593 (2014) 207–212, https://doi.org/10.1016/j.jallcom.2014.01.079.

[24] A. Korneva, B. Straumal, A. Gornakova, A. Kilmametov, Ł. Gondek, L. Lityńska-Dobrzyńska, R. Chulist, M. Pomorska, P. Zięba, Formation and thermal stability of the ω-phase in Ti–Nb and Ti–Mo alloys subjected to HPT, Materials 15 (2022) 4136, https://doi.org/10.3390/ma15124136.

[25] Á. Révész, E. Schafler, Z.S. Kovács, Structural anisotropy in a $Zr_{57}Ti_5Cu_{20}Al_{10}Ni_8$ bulk metallic glass deformed by high pressure torsion at room temperature, Appl. Phys. Lett. 92 (2008) 011910, https://doi.org/10.1063/1.2830992.

[26] Z.S. Kovács, E. Schafler, Á. Révész, Volume changes in Vitreloy bulk metallic glass during room temperature high-pressure torsion, J. Mater. Res. 23 (2008) 3409–3414, https://doi.org/10.1557/JMR.2008.0416.

[27] W. Dmowski, Y. Yokoyama, A. Chuang, Y. Ren, M. Umemoto, K. Tsuchiya, A. Inoue, T. Egami, Structural rejuvenation in a bulk metallic glass induced by severe plastic deformation, Acta Mater. 58 (2010) 429–438, https://doi.org/10.1016/j.actamat.2009.09.021.

[28] S.D. Feng, W. Jiao, Q. Jing, L. Qi, S.P. Pan, G. Li, M.Z. Ma, W.H. Wang, R.P. Liu, Structural evolution of nanoscale metallic glasses during high-pressure torsion: A molecular dynamics analysis, Sci. Rep. 6 (2016) 36627, https://doi.org/10.1038/srep36627.

[29] K. Nakazawa, S. Lee, K. Niitsu, M. Kameyama, T. Sannomiya, S. Kohara, K. Mitsuishi, K. Tsuchiya, Nanoscale strain mapping and symmetry analysis of $Zr_{50}Cu_{40}Al_{10}$ metallic glass rejuvenated by high-pressure torsion via 4D scanning transmission electron microscopy, J. Non Cryst. Solids 606 (2023) 122197, https://doi.org/10.1016/j.jnoncrysol.2023.122197.

[30] C. Ebner, B. Escher, C. Gammer, J. Eckert, S. Pauly, C. Rentenberger, Structural and mechanical characterization of heterogeneities in a CuZr-based bulk metallic glass processed by high pressure torsion, Acta Mater. 160 (2018) 147–157, https://doi.org/10.1016/j.actamat.2018.08.032.

[31] A. Jain, Y. Prabhu, D. Gunderov, J. Bhatt, Micro-indentation-induced deformation studies on high-pressure-torsion-processed $Zr_{62}Cu_{22}Al_{10}Fe_5Dy_1$ metallic glass, J. Mater. Eng. Perform. 33 (2024) 256–263, https://doi.org/10.1007/s11665-023-07933-2.

[32] G. Yang, L. Liu, J. Yi, J. Li, L. Kong, Outside-in disintegration of medium-range order in nano metallic glasses during torsion deformation revealed by molecular dynamics simulations, J. Non Cryst. Solids 595 (2022) 121827, https://doi.org/10.1016/j.jnoncrysol.2022.121827.

[33] M. Stückler, S. Wurster, M. Alfreider, M. Zawodzki, H. Krenn, A. Bachmaier, Magnetic properties of a high-pressure torsion deformed Co-Zr alloy martin, Nanomaterials 13 (2023) 2280, https://doi.org/10.3390/nano13162280.

[34] Z.S. Kovács, P. Henits, A.P. Zhilyaev, Á. Révész, Deformation induced primary crystallization in a thermally non-primary crystallizing amorphous $Al_{85}Ce_8Ni_5Co_2$ alloy, Scr. Mater. 54 (2006) 1733–1737, https://doi.org/10.1016/j.scriptamat.2006.02.004.

[35] Á. Révész, S. Hóbor, P.J. Szabó, A.P. Zhilyaev, Z.S. Kovács, Deformation induced crystallization in an amorphous Cu60Zr20Ti20 alloy by high pressure torsion, Mater. Sci. Eng.: A. 460–461 (2007) 459–463, https://doi.org/10.1016/j.msea.2007.01.081.

[36] S. Hóbor, Á. Révész, P.J. Szabó, A.P. Zhilyaev, V. Kovács Kis, J.L. Lábár, Z. S. Kovács, High pressure torsion of amorphous $Cu_{60}Zr_{30}Ti_{10}$ alloy, J. Appl. Phys. 104 (2008) 033525, https://doi.org/10.1063/1.2964115.

[37] C. Ebner, S. Pauly, J. Eckert, C. Rentenberger, Effect of mechanically induced structural rejuvenation on the deformation behaviour of CuZr based bulk metallic glass, Mater. Sci. Eng. A 773 (2020) 138848, https://doi.org/10.1016/j.msea.2019.138848.

[38] Á. Révész, P. Henits, Z.S. Kovács, Structural changes in Zr-based bulk metallic glasses deformed by high pressure torsion, J. Alloy. Compd. 495 (2010) 338–340, https://doi.org/10.1016/j.jallcom.2009.10.175.

[39] K. Edalati, Y. Yokoyama, Z. Horita, High-pressure torsion of machining chips and bulk discs of amorphous $Zr_{50}Cu_{30}Al_{10}Ni_{10}$, Mater. Trans. 51 (2010) 23–26, https://doi.org/10.2320/matertrans.MB200914.

[40] C.B. Scruby, An introduction to acoustic emission, J. Phys. E Sci. Instrum. 20 (1987) 946–953, https://doi.org/10.1088/0022-3735/20/8/001.

[41] C.R. Heiple, S.H. Carpenter, Acoustic emission produced by deformation of metals and alloys, A review, J. Acoust. Emiss. 6 (1987) 177–204.

[42] F.H. Dalla Torre, D. Klaumünzer, R. Maaß, J.F. Löffler, Stick–slip behavior of serrated flow during inhomogeneous deformation of bulk metallic glasses, Acta Mater. 58 (2010) 3742–3750, https://doi.org/10.1016/j.actamat.2010.03.011.

[43] A.Y. Vinogradov, V.A. Khonik, Kinetics of shear banding in a bulk metallic glass monitored by acoustic emission measurements, Phil. Mag. 84 (2004) 2147–2166, https://doi.org/10.1080/14786430410001678217.

[44] A. Lazarev, A. Vinogradov, S. Hasimotho, Comparative analysis of inhomogeneous plastic flow in bulk and ribbon metallic glasses monitored by acoustic emission, J. Alloy. Compd. 504 (2010) S60–S64, https://doi.org/10.1016/j.jallcom.2010.02.076.

[45] Z.S. Kovács, M. Ezzeldien, K. Máthis, P. Ispánovity, F. Chmelík, J. Lendvai, Statistical analysis of acoustic emission events in torsional deformation of a Vitreloy bulk metallic glass, Acta Mater. 70 (2014) 113–122, https://doi.org/10.1016/j.actamat.2014.02.019.

[46] H. Guo, P.F. Yan, Y.B. Wang, J. Tan, Z.F. Zhang, M.L. Sui, E. Ma, Tensile ductility and necking of metallic glass, Nat. Mater. 6 (2007) 735–739, https://doi.org/10.1038/nmat1984.

[47] C.A. Volkert, A. Donohue, F. Spaepen, Effect of sample size on deformation in amorphous metals, J. Appl. Phys. 103 (2008) 083539, https://doi.org/10.1063/1.2884584.

[48] D. Jang, J.R. Greer, Transition from a strong-yet-brittle to a stronger-and-ductile state by size reduction of metallic glasses, Nat. Mater. 9 (2010) 215–219, https://doi.org/10.1038/nmat2622.
[49] A. Dubach, R. Raghavan, J.F. Löffler, J. Michler, U. Ramamurty, Micropillar compression studies on a bulk metallic glass in different structural states, Scr. Mater. 60 (2009) 567–570, https://doi.org/10.1016/j.scriptamat.2008.12.013.
[50] O.V. Kuzmin, Y.T. Pei, C.Q. Chen, J.T.M. De Hosson, Intrinsic and extrinsic size effects in the deformation of metallic glass nanopillars, Acta Mater. 60 (2012) 889–898, https://doi.org/10.1016/j.actamat.2011.11.023.
[51] R. Qu, D. Tönnies, L. Tian, Z. Liu, Z. Zhang, C.A. Volkert, Size-dependent failure of the strongest bulk metallic glass, Acta Mater. 178 (2019) 249–262, https://doi.org/10.1016/j.actamat.2019.08.019.
[52] P.D. Ispánovity, D. Ugi, G. Péterffy, M. Knapek, S.Z. Kalácska, D. Tüzes, Z. Dankházi, K. Máthis, F. Chmelík, I. Groma, Dislocation avalanches are like earthquakes on the micron scale, Nat. Commun. 13 (2022) 1975, https://doi.org/10.1038/s41467-022-29044-7.
[53] T. Arjmandabasi, D. Ugi, Á. Révész, E. Schafler, D.J. Browne, Z.S. Kovács, In-situ compression with acoustic emission detection of high pressure torsion deformed $Cu_{38}Zr_{54}Al_8$ metallic glass micropillars, J. Alloy. Compd. 965 (2023) 171295, https://doi.org/10.1016/j.jallcom.2023.171295.
[54] Á. Révész, T. Arjmandabasi, E. Schafler, D.J. Browne, Z.S. Kovács, Comprehensive thermal analysis of a high stability Cu–Zr–Al bulk metallic glass subjected to high-pressure torsion, J. Therm. Anal. Calorim. 148 (2023) 2323–2334, https://doi.org/10.1007/s10973-022-11875-7.
[55] Z.S. Czigány, V.K. Kis, Acquisition and evaluation procedure to improve the accuracy of SAED, Microsc. Res. Tech. 86 (2023) 144–156, https://doi.org/10.1002/jemt.24229.
[56] Á. Hegyi, P.D. Ispánovity, M. Knapek, D. Tüzes, K. Máthis, F. Chmelík, Z. Dankházi, G. Varga, I. Groma, Micron-scale deformation: A coupled in situ study of strain bursts and acoustic emission, Microsc. Microanal. 23 (2017) 1076–1081, https://doi.org/10.1017/S1431927617012594.
[57] K. Hajlaoui, T. Benameur, G. Vaughan, A.R. Yavari, Thermal expansion and indentation-induced free volume in Zr-based metallic glasses measured by real-time diffraction using synchrotron radiation, Scr. Mater. 51 (2004) 843–848, https://doi.org/10.1016/j.scriptamat.2004.07.008.
[58] A.R. Yavari, A.L. Moulec, A. Inoue, N. Nishiyama, N. Lupu, E. Matsubara, W. J. Botta, G. Vaughan, M.D. Michiel, Å. Kvick, Excess free volume in metallic glasses measured by X-ray diffraction, Acta Mater. 53 (2005) 1611–1619, https://doi.org/10.1016/j.actamat.2004.12.011.
[59] M. Li, C. Yan, X. Wang, S. Yang, F. Xue, Cryogenic thermal cycling induced simultaneous improvement of strength and ductility in a Zr-based bulk metallic glass composite, J. Mater. Res. Technol. 29 (2024) 4697–4701, https://doi.org/10.1016/j.jmrt.2024.02.200.
[60] M. Karsai, K. Kaski, A.L. Barabási, J. Kertész, Universal features of correlated bursty behaviour, Sci. Rep. 2 (2012) 397, https://doi.org/10.1038/srep00397.
[61] S. Pomes, N. Adachi, M. Wakeda, T. Ohmura, Comparative analysis of nanoindentation-induced incipient deformation of zirconium-based bulk metallic glass in various structural states, Intermetallics 168 (2024) 108269, https://doi.org/10.1016/j.intermet.2024.108269.
[62] S. Zhang, J. Zhou, J. Geng, Y. Yang, P. Jin, B. Shi, Rejuvenation of a deformed metallic glass dominated by immature shear band zones during cryogenic thermal cycling, Phys. Rev. B 109 (2024) 104205, https://doi.org/10.1103/PhysRevB.109.104205.
[63] M. Tan, Y. Wang, F. Wang, Y. Gao, Y. Huang, Y. Wu, C. Jin, Y. Sun, C. Kursun, J. Wang, J. Huo, M. Gao, Rejuvenation induced suppression of crystallization in one La-based metallic glass by ultraslow cold rolling, J. Non Cryst. Solids 636 (2024) 123012, https://doi.org/10.1016/j.jnoncrysol.2024.123012.
[64] F. Spaepen, A microscopic mechanism for steady state inhomogeneous flow in metallic glasses, Acta Metall. 25 (1977) 407–415, https://doi.org/10.1016/0001-6160(77)90232-2.
[65] K.E. Avila, V.H. Vardanyan, T. Zhu, S. Küchemann, M. Smaga, H.M. Urbassek, Plasticity in cyclic indentation of a Cu-Zr-based bulk metallic glass after tensile loading: An experimental and molecular dynamics simulation study, J. Non Cryst. Solids 617 (2023) 122486, https://doi.org/10.1016/j.jnoncrysol.2023.122486.